

Flow geometry in a sunspot penumbra

R. Schlichenmaier and W. Schmidt

Kiepenheuer-Institut für Sonnenphysik, Schöneckstrasse 6, 79104 Freiburg, Germany (schliche/wolfgang @kis.uni-freiburg.de)

Received 25 January 2000 / Accepted 10 April 2000

Abstract. We have measured the material flow in the penumbra of a large symmetric sunspot during the passage of the spot across the solar meridian. The line-of-sight velocity field has been obtained from Doppler measurements in a Fe II line using a filter spectrometer with a large field of view. From data sets taken on different days, i.e. at different view angles, we have reconstructed the magnitude and orientation of the penumbral flow field in the deep photosphere. We find upflows near the inner and downflows at the outer boundary of the penumbra with nearly horizontal outflow in between. From our measurements we derive the following flow geometry: narrow upflow channels rise at different penumbral radii, they bend outwards with a nearly horizontal outflow, and are finally tilted a few degrees downwards at the outer penumbral boundary, but still inside the spot. The flow reaches its maximum speed of about 3.5 km s^{-1} in the outer part of the penumbra. Our findings are a significant step towards an understanding of the mass balance of the Evershed flow. The proposed geometry is consistent with recent numerical models of penumbral filaments.

Key words: Sun: photosphere – Sun: sunspots – Sun: magnetic fields

1. Introduction

The transition between the umbra and the penumbra of a sunspot is characterized by the steep increase in intensity, and by the onset of vigorous material motions with a strong horizontal, radially outward pointing component, the Evershed flow. In the recent decades the Evershed flow was subject of numerous investigations at ever increasing spatial resolution. Nevertheless, many aspects of the flow remain unclear, and after all we still await a self-consistent theoretical model of the penumbra.

The most important characteristic of the Evershed effect is that photospheric lines are not only Doppler-shifted, indicating a radial outflow, but also show a line asymmetry (Bumba 1960; Servajean 1961; Holmes 1963; Maltby 1964). Systematic observations with various absorption lines reveal that line shifts as well as their asymmetries depend sensitively on the formation height of the line: the higher the line core is formed the

smaller the line shift and the larger the line asymmetry (Stellmacher & Wiehr 1980; Ichimoto 1987, 1988; Balthasar et al. 1997). The most convincing interpretation of these observations is in terms of a two “component” model: an unshifted or slightly shifted main component and a line satellite, i.e. a Doppler-shifted weaker component (e.g. Schröter 1967¹). The latter stems from a spatially unresolved flow channel (Wiehr 1994) which is elevated a few hundred km with respect to the continuum (Rimmele 1995). In this work we confirm this picture except that we find that the flow is less elevated, i.e. is concentrated in the very deep photosphere.

Also, it is observed that the limb side penumbra shows a different line asymmetry than the center side penumbra (Schröter 1965; Rimmele 1995). In terms of flow channels, this observation can be understood if the flow is not quite horizontal, but slightly inclined upwards, as it was reported e.g. by Schröter (1965), Tittle et al. (1993), and Shine et al. (1994).

Rimmele (1995) pointed out that the contribution functions of photospheric absorption lines are wider than the flow channel itself, i.e. plasma above and below the flow channel significantly contributes to the measured line profile. Assuming that the surrounding plasma is at rest, we expect that the measured Doppler velocities are smaller than the actual flow velocity (even if the flow is spatially resolved). This would explain that measured Doppler velocities are smaller than those predicted by theoretical models.

The strong radial outflow across the penumbra raises the question about the nature of sources and sinks of the moving gas (mass balance). Schlichenmaier et al. (1998a,b) approached this problem theoretically and postulated the “moving” tube model: a thin magnetic flux tube which *moves* in the penumbra. Here, the cool horizontal flow is fed by a hot upflow (the source) which cools as it reaches the photospheric layers; at the outer penumbral boundary this flow continues to stream upward to the magnetic canopy which surrounds the sunspot, and thereby guarantees the mass balance. Observations from Johansson (1993), Rimmele (1995), and Schlichenmaier & Schmidt (1999, hereafter: paper I) indicate the existence of hot upflow channels in the inner penumbra and are thus consistent with the

¹ For very strong lines, a second line satellite is observed which most probably is the signature of the inverse Evershed effect.

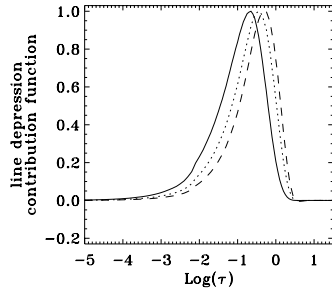
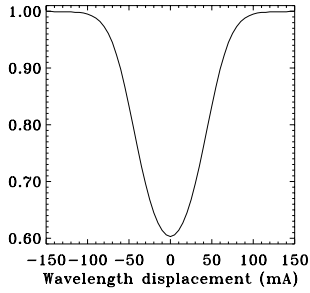


Fig. 1. Left panel: Profile of the Fe II 542.5 nm line, computed for a spectral resolution of 2.5 pm and a standard atmosphere for the quiet Sun; right panel: contribution function for the line core (solid), the wings at half maximum (dotted) and the outer wings (dashed).

moving tube model. However, at the outer penumbral boundary, observations are unclear about the behaviour of the flow. Depending on the observational method and on the spectral line used, ambiguous results are obtained: From the zero-crossing shift of Stokes–V profiles (which stem from the upper photosphere) Solanki et al. (1994, see also Solanki et al. 1999) infer that some 20% of the flow does indeed continue upwards towards the magnetic canopy, as it is predicted by the moving tube model. On the other hand, using absorption lines which form in the mid-photosphere, numerous observers have confirmed the work of Evershed (1909): the line shift and also the line asymmetry ceases abruptly at the outer boundary of the penumbra (e.g. Börner & Kneer 1992; Wiehr & Degenhardt 1994; Wiehr 1996; Balthasar et al. 1996). Finally, in the deepest photospheric layers, observational evidence for the existence of a few isolated downflow patches was presented (c.f., Westendorp Plaza et al. 1997).

In the present work, we concentrate on the penumbral flow field of the deep photosphere in order to (i) disentangle the ambiguities of the previous observations, (ii) verify the moving tube model, and (iii) address the question of mass balance. This is done by inferring the radial dependence of the flow inclination and the flow velocity. Only Schröter (1965) previously performed a similar analysis. He observed an isolated symmetric sunspot during its disk passage on 12 subsequent days in 1962 with the slit always oriented towards disk center. He derived an inclination angle (with respect to the solar surface) for the Evershed flow that decreased from $30^\circ \pm 8^\circ$ in the inner penumbra to $12^\circ \pm 7^\circ$ at the outer penumbral boundary. The inferred velocity reached a maximum of $(1.9 \pm 0.1) \text{ km s}^{-1}$ at 80% of the spot’s radius. Today, with the help of two-dimensional spectroscopy and an excellent observing site, we can acquire a data set of superior quality. Since we can rely on two-dimensional velocity maps (see Sect. 2), we are able to infer the flow geometry of a penumbra from one single spectrum (see Sect. 4) instead of having to combine datasets from 12 different days.

We will prove the capability and validity of our method by demonstrating the consistency of four inferred penumbral flow fields of an isolated, round, and stable sunspot. These flow fields were obtained under four different view angles, i.e. by observing the spot on four subsequent days. In contrast to the work

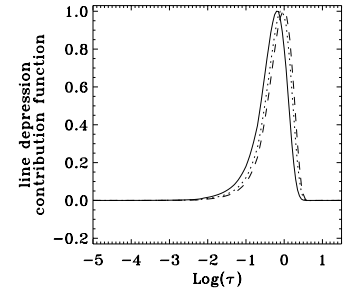
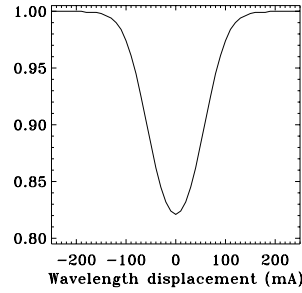


Fig. 2. Same as Fig. 1, for the C I 538.0 nm line.

of Schröter we concentrate on the deepest layers of the penumbral photosphere by selecting appropriate absorption lines (see Sect. 2).

Sect. 2 describes the data and the methods used for the data reduction. In Sect. 3 we study the influence of varying seeing during the wavelength scan on the line profiles. In Sect. 4 we present velocity maps of a sunspot, introduce the method used to analyze the flow geometry, and present results of our analysis. In the concluding Sect. 5 we discuss our findings.

2. Observations and data reduction

2.1. Selection of absorption lines

As mentioned in the introduction, the largest line core shift is present for lines that are formed in the deepest part of the photosphere. Such lines should be capable to provide information about the proposed, low-lying flow channels. For our observations we therefore have chosen two lines, which originate in the deep photosphere: an ionized iron line at 542.5 nm and a weak line of neutral carbon at a wavelength of 538.0 nm.

Fe II 542.5 nm: This is a temperature sensitive “hot” line with a high excitation potential of 3.2 eV and a Landé factor of $g_{\text{eff}} = 1.25$. The right panel of Fig. 1 shows the contribution functions (Grossmann-Doerth 1994) for the line core (solid line), the wing at half maximum (dotted line), and the far line wing (dashed line). For the computations we have used a standard atmospheric model of the quiet Sun (Holweger & Müller 1974), and we took into consideration a spectral resolution of 2.5 pm. The contribution function peaks at $\log \tau = -0.7$, and the line forms predominantly in layers below $\log \tau = -1$, corresponding to $h = 130 \text{ km}$ above $\log \tau(500 \text{ nm}) = 0$. It forms even deeper when magnetic fields are present.

C I 538.0 nm: This weak line has an extremely high excitation potential of 7.3 eV and a magnetic sensitivity corresponding to $g = 1$. Fig. 2 demonstrates that it is formed in the deepest accessible layers of the quiet sun atmosphere: the contribution function of the line core peaks around $\log \tau = -0.2$ (i.e., $h = 25 \text{ km}$), with a full width at half maximum reaching from below the continuum up to $\log \tau = -0.7$ (i.e., $h = 100 \text{ km}$).

The magnetic sensitivity of these lines is rather small, and the sunspot magnetic field together with the potential effects of instrumental polarization should not cause significant line shifts. The Zeeman effect alone does not change the line position, since it causes a symmetric line broadening. It would take a rather

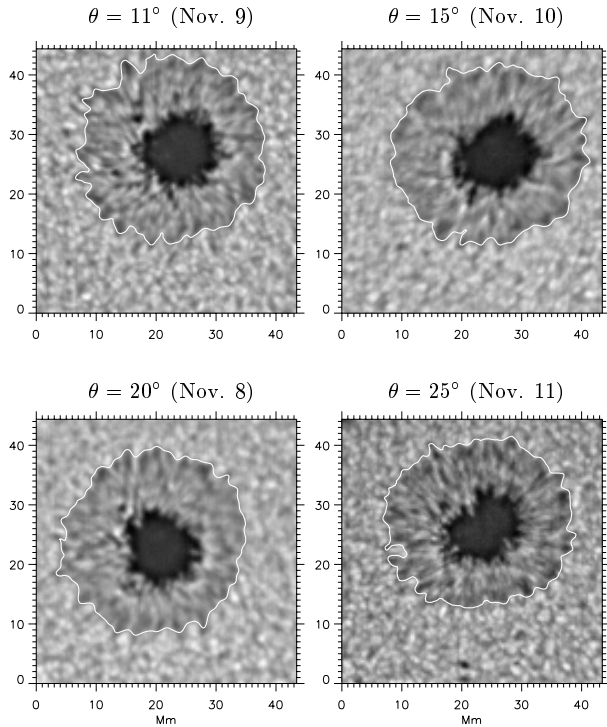


Fig. 3. Contrast enhanced intensity maps of the sunspot observed on four consecutive days. The disk positions are $\theta = 20^\circ$, 11° , 15° and 25° .

strong instrumental polarization effect to produce such a line asymmetry which then could be interpreted in terms of artificial Doppler motion (cf. Sect. 4.4).

If one calculates the line profiles for a mean penumbral atmospheric model, e.g. Ding & Fang (1989), one finds that both lines have an insignificant line depression (less than a percent). This is due to the coolness of such an atmosphere. However, we observe the presence of both lines within the penumbra with line strengths similar to the quiet photosphere. This is not surprising, since many of the bright structures reach (or even exceed) photospheric brightness (Grossmann-Doerth & Schmidt 1981; Denker 1998; Sütterlin & Wiehr 1998).

2.2. Observations

The observations have been carried out at the German Vacuum Tower Telescope in the Observatorio del Teide, Tenerife, from 8 to 11 November 1998. We used the filter spectrometer TESOS (Kentischer et al. 1998) to take two-dimensional spectra of a sunspot and its immediate surroundings. TESOS has a large field of view with a diameter of 95 arcsec and is therefore well suited for this kind of observations. The instrument was used in its low-resolution mode with a pixel size of 0.25 arcsec and a spectral resolution of 160,000. A single data set consists of 20 narrow-band filtergrams taken at equidistant positions across the spectral line. The spectral step width was 2.0 pm for both lines. Broadband images with exactly the same field of view were recorded simultaneously with each filtergram. The 0.3 nm prefilter used for the carbon line unfortunately had rather poor

transmission, so an integration time of 0.8 s was necessary (0.4 s for the ionized iron line), resulting in a measurement cadence of about 40 s for the carbon and 20 s for the iron line. Seeing conditions were fair to good during the observations and all data used for the present analysis have a spatial resolution of better than one arcsecond.

Target: We have observed an isolated round sunspot (NOAA 8578) on its passage through the central meridian, at heliocentric angles of 20° , 11° , 15° , and 25° . Fig. 3 shows examples of good continuum images, one for each day. The spot undergoes little evolution during the observations and a comparison of the penumbral flow measured on different days is therefore justified.

2.3. Data reduction

The standard procedures for flat field and dark current correction have been applied. The processing of raw data is straightforward without major complications, due to the good wavelength stability of TESOS. The correlation tracker (Schmidt & Kentischer 1995) of the VTT provided the fine pointing with an accuracy of about 0.1 arcsec, therefore a rigid alignment of the individual filtergrams within a single data set was not necessary. We applied a standard destretch algorithm to remove image distortion from the individual images. To this end we used the continuum images that had been taken with the filtergrams. Firstly, the relative orientation and image scale of the continuum images was carefully adapted to that of the filtergrams. Images of a grid target were used for that purpose. In a second step the position stability was checked (and would have been corrected, if necessary), and then the image distortion of the continuum images with respect to the mean image was determined and corrected. The sub-image displacements were then applied to the corresponding filtergrams.

2.4. Method to determine line shift

The line shift was measured at every spatial point of each spectrum to construct two-dimensional velocity maps. We applied a simple method to determine the position of the line, similar to the principles of a Fourier tachometer: the phase of the first Fourier component of the line profile is a measure of the position of the line within the measured wavelength interval. The Fourier transform $F(u)$ of the line profile $f(\lambda)$, measured in the interval $\Delta\lambda = [\lambda_1, \lambda_2]$ can be written as

$$F(u) = R(u) + iI(u),$$

$$\text{with } |F(u)| = (R^2 + I^2)^{1/2}, \text{ and } \Phi(u) = \arctan\left(\frac{I}{R}\right).$$

The line position with respect to the center of the interval is then just $\Phi(u_0)$, with the basic frequency $u_0 = 1/\Delta\lambda$. The Fourier method is best suited for symmetric profiles, since then the line position corresponds to the centre-of-gravity shift and at the same time to the line core shift of the line profile. The method is faster than other techniques and it is, by definition, very insensitive to noise. It was initially intended to serve as

a “first guess” procedure, with subsequent refinement with another method, e.g. the computation of line bisectors. We have carried out extensive tests, based on 2D spectra from TESOS and also slit spectra taken with the high-resolution Echelle spectrograph, and found very good agreement between the Fourier and other methods, well within the velocity resolution of our data. As it is expected for weak deep-forming absorption lines, our measured profiles do not show significant asymmetries. Therefore, the Fourier method is well suited and was used throughout the analysis. The line shifts, $\Delta\lambda$, were converted to Doppler velocities according to the Doppler equation $\Delta\lambda/\lambda = v_D/c$, where c is the speed of light and v_D is the Doppler velocity. We used the average velocity of the granulation outside the immediate vicinity of the spot as a reference. In order to account for the convective blue shift (Balthasar 1984), we subtracted a value of 0.4 km s^{-1} from this average. The most suitable reference point for the velocity would have been the umbra, which is known to be at rest (on average), but both the iron and the carbon lines are virtually absent in the umbra, due to their temperature sensitivity, and no reliable line positions can be measured. In addition the Fe II line shows a blend in the red wing.

We would like to mention that scattered light from the surrounding granulation causes a slight blue-asymmetry of the line profiles in the penumbra. This systematic effect has some influence on the velocity calibration. Assuming a stray light level of 10%, we estimate a blue shift of some 50 m s^{-1} (cf., Sect. 4.5).

3. Seeing-induced shifts of the line profile

Special care has to be taken when selecting “good” spectra. It is most important that the filtergrams are recorded during *constant* seeing conditions. In this section we demonstrate that variable seeing conditions during the scan can produce artificial Doppler shifts of the line. Seeing changes during the scan change the rms contrast of the image, and hence lead to an intensity change in dark and bright structures: During instances of ‘bad’ seeing the continuum intensity of bright structure, e.g. granules, decreases as compared to instances of ‘good’ seeing, and vice versa for dark structures, e.g. dark granular lanes. Such changes falsify the line profile, and may lead to artificial, *seeing-induced*, shifts of the line core.

Let us assume that the rms intensity fluctuations, s , increase linearly while the absorption line is scanned from the blue to the red. In this case the blue continuum of a bright structure has a smaller intensity than the red continuum, and the line profile is tilted such the line core is shifted towards the blue. For a dark structure the opposite is true, the line core apparently shifts towards the red.

3.1. Simulated spectra under variable seeing conditions

In order to estimate the effects of variable seeing conditions of the Doppler velocities of the line core we have performed a simple numerical experiment. We approximate the Fe II line by a Gaussian profile, which has the same line depression, d , and full width at half maximum (FWHM), σ , as the corresponding

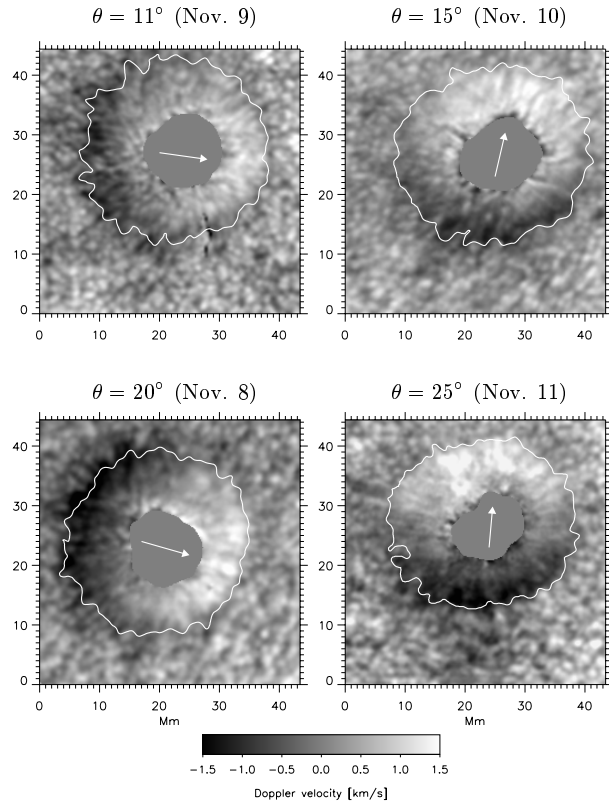


Fig. 4. Line-of-sight velocity maps, derived from the Fe II 542.5 nm line. The maps correspond to the continuum images shown in Fig. 3 with disk positions of $\theta = 20^\circ, 11^\circ, 15^\circ, 25^\circ$. The arrows point to disk center. Umbral velocities have been set to zero. Velocities ranging from -1.5 km s^{-1} (red-shift) to $+1.5 \text{ km s}^{-1}$ (blue-shift) are displayed.

line from the Liège Atlas, i.e., $d = 40\%$ and $\sigma = 8 \text{ pm}$. We use the rms intensity contrast, s , of the continuum images as a measure of the seeing conditions. In order to model the spatial dependence of the intensity, $I = I(x)$, of the granulation, we assume: $I(x) = I_0 + A \cdot \sin(x)$. The amplitude, A , of the intensity variation is related to the rms fluctuations by: $A = \sqrt{2} \cdot s$.

If we assume a linear increase of s by $\Delta s = 0.01$ during the scan, and measure the line core shift using the method described in Sect. 2.4, we obtain a blue-shift for the bright structures of 70 m s^{-1} and a red-shift for the dark structures of 70 m s^{-1} . The line shift turns out to be proportional to s , i.e. a larger change of the rms contrast would increase the artificial line shift. The amount of the artificial shift depends critically on the line depression: Weaker lines are stronger influenced than stronger ones. We find that the dependence of the line core shift is approximately inversely proportional to the line depression.

Arbitrary seeing fluctuations, δs , of the seeing do not lead to a systematic shift of the line, but add to the noise of the line profile. This again stresses the necessity for the noise insensitive method of Sect. 2.4 that we used to determine the line core shift.

The spectra used for the present investigation have been selected by evaluating the rms-contrast of the granulation within the broadband images as a function of wavelength (for each

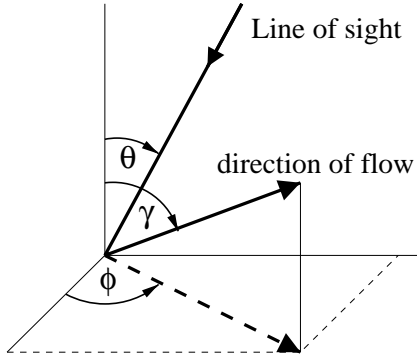


Fig. 5. The heliocentric angle, θ , and the inclination angle, γ , are measured with respect to the surface normal. The azimuth, ϕ , is defined such that $\phi = 90^\circ$ points towards disk center.

filtergram TESOS records a simultaneous broadband white light image). Except for November 10, we used spectra in which the overall trend of the rms-contrast, Δs , during the scan and individual fluctuations, δs , were less than 0.005. For November 10 our best spectrum has fluctuation of the rms-contrast of $\delta s = 0.008$ and a mean decrease of the rms-contrast during the scan of $\Delta s = 0.01$ and is therefore somewhat less reliable.

Since it turned out that the neutral carbon line is very sensitive to seeing variation, we finally refrained from including this line into the present analysis. For the carbon velocity map that we presented in paper I, the rms-contrast increased by almost $\Delta s = 0.8\%$ as the line was scanned from the blue to the red. We applied the simulation to the carbon line, and found that such an increase in the rms-contrast leads to an artificial shift of the line core in dark structures towards the red by some 190 m s^{-1} and the line core of bright structures to the blue by 190 m s^{-1} . In spite of this effect, the main results of paper I remain valid, but the amplitudes of the absolute up- and downflow velocities overestimated by some 200 m s^{-1} .

4. Results

4.1. Velocity maps

Fig. 4 displays the best line-of-sight velocity maps for each of the four observing days, measured in the Fe II 542.5 nm line. The orientation of the spot on the solar disk is indicated with arrows pointing towards disk center. Negative values correspond to redshifts. Since the red wing of the line is blended in the cool umbra, no line positions have been measured there and the velocity has been set to zero for the whole umbra. The heliocentric angle of the spot increases from the upper left panel to the lower right panel. The typical feature of the radial Evershed flow consists of the azimuthal asymmetry, i.e., the velocity maps show a blue-shift towards disk center and a red-shift towards the solar limb.

Before entering in the detailed analysis of the flow geometry, we start with a few remarks concerning Fig. 4: The upper left panel displays the velocity map at a rather small heliocentric angle of 11° . In the inner penumbra, upflows are present at all azimuths. Secondly, viewing the outer penumbral boundary at the disk center side of the spot, the LOS component of the ve-

locity, $v = v(r)$, has a minimum, and, moreover, this minimum has very small and in some cases negative values. This indicates that the Evershed effect apparently disappears at the outer penumbral boundary, and the negative values give a hint, that the flow might be inclined slightly downwards at the outer penumbral boundary. The systematic investigation in the following sections will confirm this first qualitative impression.

4.2. Analysis of the flow geometry

For the analysis of the flow geometry, we assume that the physical flow field does not depend on the azimuth, i.e., we assume axial symmetry. This implies that azimuthal velocity variations are purely due to line-of-sight effects. Moreover, when we compare the velocity fields of the 4 different days, we tacitly assume that the flow field of the spot does not change during the four days of observation. The latter is justified by noting that the appearance of the spot does not change in that period.

We make use of the highly symmetric appearance of the observed sunspot and investigate velocities as a function of radius and azimuth, measured from the center of the spot. The line-of-sight measurement, v^{LOS} , is related to the material flow on the Sun through

$$v^{\text{LOS}}(r, \phi) = v_0(r) \cdot [\sin \theta \cdot \sin \phi \cdot \sin \gamma(r) + \cos \theta \cdot \cos \gamma(r)] \quad (1)$$

(e.g. Schröter 1967), where v_0 is the flow velocity, θ is the heliocentric angle of the sunspot, γ denotes the inclination angle of the flow with respect to the surface normal and ϕ is the azimuth angle of the sunspot, with $\phi = 90^\circ$ pointing to disk center (see Fig. 5).

From the measurements we extract the vertical and horizontal components of the line-of-sight velocity, since only the horizontal component shows an azimuthal variation. The vertical component does not depend on azimuth and v_{\perp}^{LOS} equals the azimuthal mean of the line-of-sight velocity. Using Eq. (1), the vertical component of the line-of-sight velocity is given by

$$v_{\perp}^{\text{LOS}}(r) = v_0 \cdot \cos \theta \cdot \cos \gamma(r) = \langle v^{\text{LOS}}(r, \phi) \rangle_{\phi}, \quad (2)$$

and the horizontal component is described by

$$\begin{aligned} v_{\parallel}^{\text{LOS}}(r) &= v_0 \sin \theta \sin \gamma(r) \cdot \sin \phi = v_{\parallel,0}^{\text{LOS}} \cdot \sin \phi \\ &= v^{\text{LOS}}(r, \phi) - \langle v^{\text{LOS}}(r, \phi) \rangle_{\phi}, \end{aligned} \quad (3)$$

with $v_{\parallel,0}^{\text{LOS}}$ being the amplitude of the azimuthal sinusoidal variation. The inclination angle, $\gamma(r)$, can be inferred from $v_{\parallel,0}^{\text{LOS}}(r)$ and $v_{\perp}^{\text{LOS}}(r)$ using Eq. (1):

$$\gamma(r) = \arctan \left(\frac{v_{\parallel,0}^{\text{LOS}}(r)}{v_{\perp}^{\text{LOS}}(r) \cdot \tan \theta} \right). \quad (4)$$

The absolute flow velocity, $v_0(r)$, is now given as

$$v_0(r) = \frac{v_{\perp}^{\text{LOS}}(r)}{\cos \theta \cdot \cos \gamma(r)} \quad (5)$$

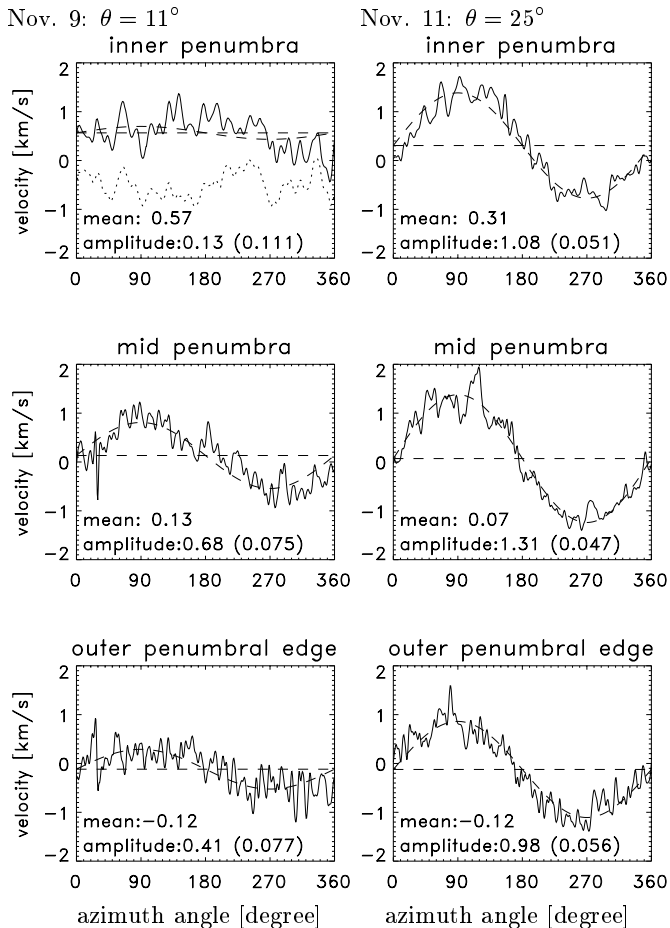


Fig. 6. Azimuthal slices of velocity maps for the smallest heliocentric angle, $\theta = 11^\circ$ (left column), and the largest heliocentric angle, $\theta = 25^\circ$ (right column), measured at different penumbral radii. In each panel, the azimuthal mean, corresponding to v_{\perp}^{LOS} , and the amplitude of the sinusoidal least-square-fit, $v_{\parallel,0}^{\text{LOS}}$, are given together with the standard deviation for the fit in brackets.

4.3. Azimuthal slices

In order to apply the above formulae to our data set, we fit ellipses to the inner and outer penumbral boundaries. For each radial position in between, ellipses are defined such that the form of the ellipse evolves continuously from the inner to the outer ellipse. The outer ellipse is extended to the adjacent granulation by increasing its radius.

Fig. 6 shows some examples of the line-of-sight velocity as a function of azimuth, measured at three different radii: at the inner, the mid, and the outer penumbra. In the left column the heliocentric angle is 11° and in the right column the position angle is 25° . The sinusoidal behavior demonstrates the presence of a horizontal component, while the LOS component of the vertical velocity component is just the azimuthal mean, indicated by a horizontal dashed line. The amplitude of the azimuthal variation, $v_{\parallel,0}^{\text{LOS}}$, is determined by performing a least-square sinusoidal fit, which is overplotted in each panel (dashed line). The values of the azimuthal mean and the amplitude of the azimuthal variation are given in each panel in units of km s^{-1} . The

Table 1. Horizontal velocity for 4 different heliocentric angles. The actual horizontal velocity component of the flow is related to the corresponding LOS component by: $\max(v_{\parallel,0}(r)) = \max(v_{\parallel,0}^{\text{LOS}}(r)) / \sin \theta$

θ [$^\circ$]	11	15	20	25
$\max(v_{\parallel,0}^{\text{LOS}}(r))$ [km s^{-1}]	0.7	1.0	1.3	1.4
$\max(v_{\parallel,0}(r))$ [km s^{-1}]	3.6	3.9	3.7	3.3

value in brackets gives the χ^2 -value of the fit, i.e. essentially the mean of the squared differences between the data and the fit.

The azimuthal variation is stronger for larger position angles, and is largest for the mid penumbra in each individual column. The azimuthal mean decreases from the inner to the outer penumbra, and, in both cases, becomes negative at the outer penumbral edge. The latter indicates the presence of a flow that is slightly inclined downwards. The upper left panel shows the LOS velocities of the inner penumbra with the smallest observed heliocentric angle: The amplitude of the azimuthal variation is almost vanishing, while the azimuthal mean amounts to more than 0.5 km s^{-1} . This is a clear indication for the presence of upflows in the inner part of the penumbra. The dotted line marks the corresponding change of the intensity, and shows that upflow channels are pretty well correlated with high intensities in the white light images. Hence, we see evidence for upflow channels which transport hot sub-photospheric plasma into the penumbral photosphere.

4.4. Radial dependence of the line-of-sight velocity

In this section we investigate the horizontal and vertical components of the measured flow as a function of spot radius. The results for all four data sets are summarized in Fig. 7. The azimuthal means are plotted in the left column, and the right column shows the amplitude of the azimuthal variation as solid line, and the relative error of the least-square fit as dotted line. The latter is defined by $\epsilon(r) = \chi^2(r)/v_{\parallel,0}^{\text{LOS}}(r)$. The left end of the abscissa corresponds to the inner boundary of the penumbra, and the vertical line at some 16 Mm denotes the outer edge of the penumbra.

In all four data sets, the vertical velocity shows the same, most remarkable, qualitative behavior: It decreases within the penumbra with increasing radius, and reaches a minimum just at the outer penumbral edge. In the very inner region of the penumbra, a molecular blend in the red wing leads to an apparent red-shift of the line. Outside the sunspot, the vertical velocity increases with radial distance, and, at some 5 – 10 Mm beyond the outer penumbral edge approaches the assumed value of the convective blue-shift. Obviously, the granulation in the immediate vicinity of the sunspot is “abnormal” in the sense that the convective blue-shift is smaller there than in the quiet sun.

In accordance with previous observations, the amplitude of the azimuthal variation, $v_{\parallel,0}^{\text{LOS}}(r)$, increases with increasing position angle (from top to bottom). The maximum values to-

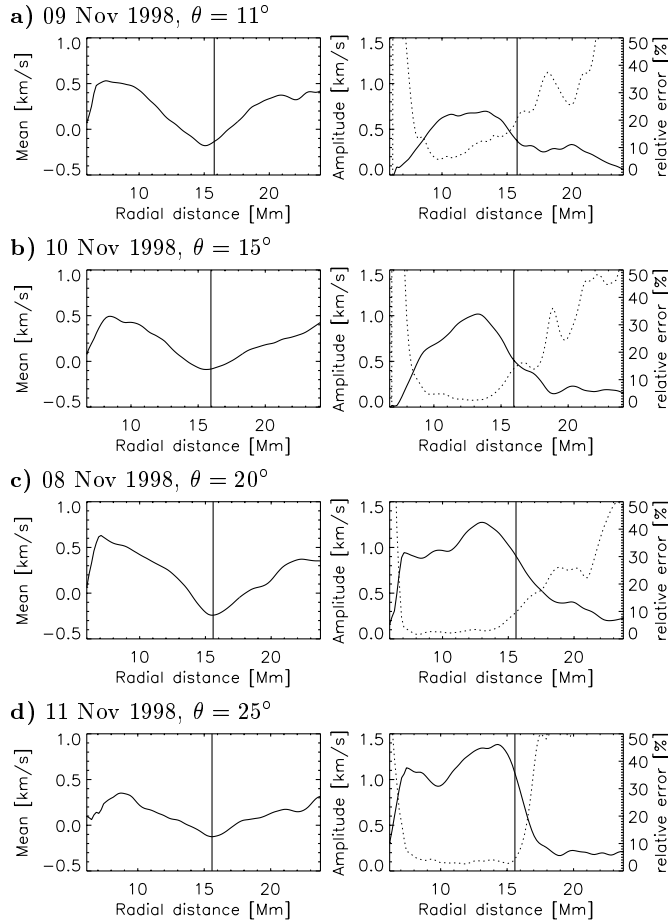


Fig. 7. Azimuthal mean and amplitude of azimuthal variation, corresponding to vertical and horizontal LOS velocities, respectively, versus radial distance from spot center for all 4 data sets. The penumbra spans from the left end of the abscissa to the vertical line at 16 Mm.

gether with the corresponding horizontal velocity component of the flow are given in Table 1. The results of the different days are consistent with each other, which reflects the validity of our method, and confirms *a-posteriori* our assumptions that the flow field is axially symmetric and that the flow field does not change significantly during the four days of observations. Averaging our data set, we obtain a mean horizontal flow velocity of $3.6 \pm 0.2 \text{ km s}^{-1}$. This horizontal flow corresponds to the “classical” Evershed flow. In accordance with other observations, e.g. Schröter (1965) and Rimmele (1995), the horizontal component reaches its maximum not at the outer penumbral edge, but within the penumbra, as it is seen in Fig. 7. We note that the spectral line that we use obviously traces the hot flow within the bright features, and at the same time it has contributions from the very deep layers of dark penumbral filaments, tracing the classical Evershed flow.

Our flow field analysis can only be applied if a horizontal flow component is present, which leads to a sufficiently large azimuthal variation. Hence, we expect small relative errors within the mid and outer penumbra and a decrease of the relative errors with increasing position angle. Outside the penumbra, the

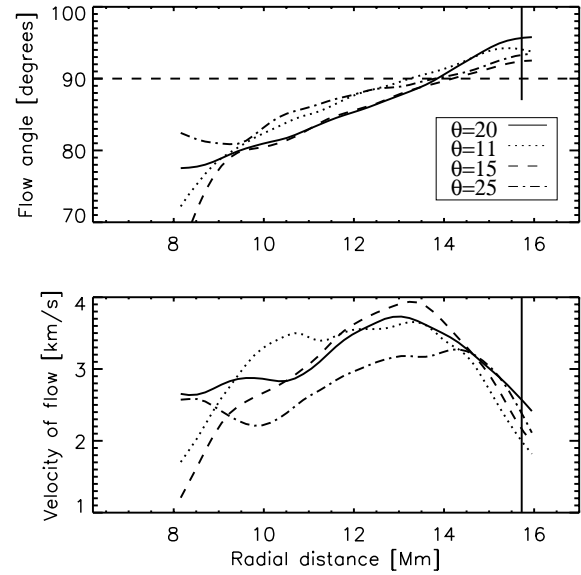


Fig. 8. Inclination angle, γ , and absolute flow velocity, v_0 , within the penumbra versus radial distance from spot center for all 4 data sets. The vertical solid line marks the averaged outer edge of the penumbra, and the left end of the abscissa corresponds to its inner boundary. The position angles are 11° (dotted), 15° (dashed), 20° (solid), and 25° (dash-dot). The flow angle is measured with respect to the surface normal, angles larger than 90° point inside the sun.

fitting errors should be large, because of the lack of a horizontal flow. The dotted lines in the right column of Fig. 7 illustrate the agreement between the sinusoidal least-square fit and the data and are consistent with these expectations. The residual error present in the mid and outer penumbra is due to the small scale velocity fluctuations which stem from the penumbral fine structure (cf., Fig. 6).

4.5. Radial dependence of inclination angle and flow speed

With the use of Eqs. (4) and (5), we calculate the inclination angle of the flow, $\gamma(r)$, and the absolute flow velocity, $v_0(r)$. As discussed in the previous section, our method only gives reliable results in the mid and outer penumbra. They are shown in Fig. 8. In all four cases, the inclination angle, plotted in the upper panel, increases with growing radial distance: the mean flow that points upwards in the inner penumbra becomes flatter for larger radii, and is slightly inclined downwards at the outer penumbral edge. Our data consistently show that a large fraction of the Evershed flow disappears below the surface at the outer penumbral edge. On average, we find an inclination angle of -4° with respect to the horizontal at the outer penumbral edge. The Wilson depression causes a slight tilt of about 3° of the penumbral “surface” (optical depth $\tau = 1$) towards the umbra. The angle between that surface and the flow therefore amounts to -7° .

The absolute inclination angle does depend on the choice of the convective blue-shift, but changing its value by $\pm 100 \text{ m s}^{-1}$ only varies γ by $\mp 2^\circ$. The existence of a downflow all around

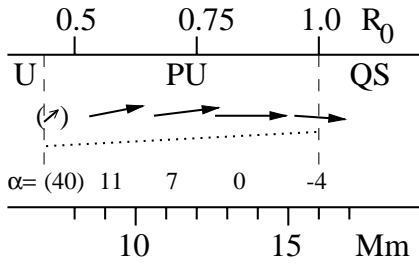


Fig. 9. Illustration of radial dependence of flow angles, $\alpha(r) = 90 - \gamma(r)$. The dotted line represents the mean $\tau = 1$ surface for a penumbra, inclined by typically 3° , due to the Wilson depression. The length of the arrows is proportional to the flow velocity. The vertical dashed lines mark the inner and outer boundary of the penumbra.

the penumbra is one of the main findings of the present work. It remains valid, even if our velocity calibration was off by $\pm 100 \text{ m s}^{-1}$. Based on the standard deviation of the least-square fit for the mean and the amplitude of the velocity, we find that the error propagation on the inclination angle results in a 1σ -error of less than 1 degree in all cases.

The lower panel of Fig. 8 displays the radial dependence of the absolute flow velocity from our four independent data sets. Although the scatter is somewhat larger than in the upper panel, the results of the different data sets are still consistent. The consistency of our results, based on four independent measurements with different view angles also confirms that the instrumental polarization together with the magnetic sensitivity of the spectral lines and scattered light do not corrupt the measurements. The flow velocity reaches its peak value within the penumbra and decreases towards the outer edge. A remark concerning the absolute flow speed should be made: whether a measured change of the line shift is due to a physical change of the flow velocity within the penumbra, or whether it is a consequence of a varying “sensitivity” of the line, e.g. due to temperature variation and/or changing geometrical height of the flow channel, cannot be decided from this data alone.

Fig. 9 gives a geometric illustration of the radial dependence of the deduced flow angles and velocities. In this sketch the angles are given with respect to the horizontal: $\alpha = 90^\circ - \gamma$. The solid arrows are mean values taken from Fig. 8. The arrow in brackets is derived from the upper left panel of Fig. 6, i.e. from the inner penumbra with a position angle of $\theta = 11^\circ$. The dotted line represents the tilt of the mean penumbral surface, assuming a typical Wilson depression.

In Fig. 9 we have assumed that the $\tau = 1$ surface of the penumbra is geometrically plane. This assumption was made for simplicity. One has to be aware that we still await a realistic model for the penumbral atmosphere and a self-consistent theoretical penumbra model: it may well be, that temperature fluctuations within the penumbral fine structure produce a $\tau = 1$ surface that has a geometric amplitude of, say, up to 100 km in depth.

5. Conclusion and discussion

We have analyzed the flow field of an isolated round sunspot on four consecutive days, during which the spot’s appearance did not change significantly. Taking advantage of the spot’s quasi-axial symmetry, we retrieved the vertical and horizontal velocity component and deduced the actual flow angle and flow velocity as a function of radial distance from spot center.

5.1. Mass balance of Evershed flow

Our investigation sheds new light on the long standing question of mass balance of the Evershed flow: We find upflows in the inner and mid penumbra that feed the outward directed component of the “classical” Evershed flow². At the outer penumbral boundary, in the deepest layers of the photosphere, we find flow channels that are slightly inclined downwards. This continuation of the Evershed flow is only visible in the deep photosphere, where our measurements are made, and this explains, why other observations using stronger absorption lines which form in higher layers, find that the Evershed flow ceases abruptly at the outer penumbral edge. Our measurements qualitatively resolve the problem of mass continuity of the Evershed flow. However, we do not attempt a quantitative estimate of the mass flow, because the variables needed for such an estimate are subject to large uncertainties, e.g. the density and temperature stratification of penumbral fine structure as well as the filling factor of the flow.

Evidence for downflows at the outer penumbra has been found previously (Westendorp et al. 1997 Stanchfield et al. (1997), but our results show, for the first time, the existence of a downflow all around the outer penumbral edge. These downflows most probably consist of magnetized plasma. As a consequence, such flows imply that some fraction of the magnetic flux returns into the solar interior. Independent support for a return flux at the outer penumbral boundary was recently proposed by Solanki et al. (1999): Comparing the expansion rate of thick and thin magnetic flux tubes, they find that a small fraction of the magnetic flux of a sunspot may return into the solar interior at the spot boundary. The fact that such a return flux was hitherto not observed with polarimetric measurements might be due to the very small inclination of -4° with respect to the horizontal on the one hand, and on the other hand one has to realize that such a reversed polarity is hidden by the overlying magnetic field which by far dominates the polarization signal, especially if one uses the “typical” Zeeman-split lines with large Landé factor, like the Fe I 630.2 nm line, which forms in the mid photosphere and has only very little contributions from the deep photospheric layers.

² Establishing the presence of upflows (which transport hot subphotospheric plasma into the photosphere) has important implications for the energy transport in penumbrae: in paper I we have estimated that they can explain the surplus brightness of the penumbra as compared to the umbra.

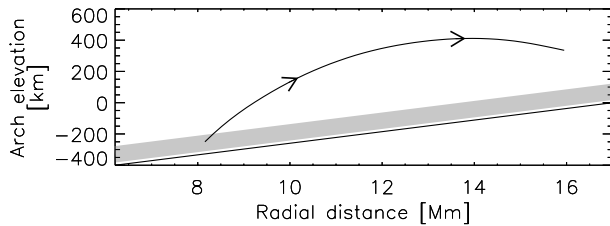


Fig. 10. Reconstructed flow channel, assuming axially symmetric flow channels. The tilted solid line represents the surface of the penumbra with a Wilson depression of 400 km. Such an arch is inconsistent with our data, since its height is much larger than the formation height (shaded area) of the used absorption line. See Fig. 11 for comparison.

5.2. Flow geometry

In the preceding section we have determined the radial dependence of the inclination angle, $\gamma = \gamma(r)$. In order to deduce the flow geometry from $\gamma(r)$ additional assumptions about the flow channels have to be made, and we discuss two different possibilities.

One may assume that all flow channels at all azimuths have the same radial shape, i.e. that the flow channels are arranged in axial symmetry with respect to the center of the spot. Then the trajectory, $h(r)$, of the flow can be reconstructed by integrating the angle, $\langle \alpha(r) \rangle = 90^\circ - \langle \gamma(r) \rangle$, according to

$$h(r) = \int_{r_0}^r \tan \langle \alpha(r') \rangle dr' ,$$

where r_0 is the radial distance of the starting point in the inner penumbra, and $\langle \alpha(r) \rangle$ is the mean angle, averaged over the 4 data sets. Fig. 10 shows the resulting radial dependence of the elevation, $h(r)$. The arch reaches up to some 400 km above the quiet sun photosphere, and has an elevation of some 300 km at the outer penumbral edge. This flow geometry would be in accordance with the *thin elevated channels* proposed by Rimmele (1995)³. However, even though this arch reproduces our measured dependence of $\gamma(r)$, it is inconsistent with our data for the following reasons: 1) The used spectral line (Fe II 542.5 nm) mainly forms in the first 100 km above the continuum (cf. Sect. 2.1), and the flow that we infer from our observation must exist within that depth range. 2) The continuation of such an elevated arch should be observable beyond the outer penumbral edge, but we find that it disappears there. For these reasons, we find *a-posteriori* that the above assumption (all flow channels have the same radial shape) is inconsistent with our observation.

Instead, let us assume a geometry as shown in Fig. 11: Upflow channels occur at various radial distances, each at a different azimuth angle. At an elevation of some 100 km, each upflow bends essentially horizontal and forms the footpoint of a radial outflow channel. An azimuthal slice somewhere in the mid penumbra averages over horizontal channels and over channels that have their upflow footpoint just on the slice. Hence the

³ Except that Rimmele does not find indications for a downward component at the outer penumbral boundary.

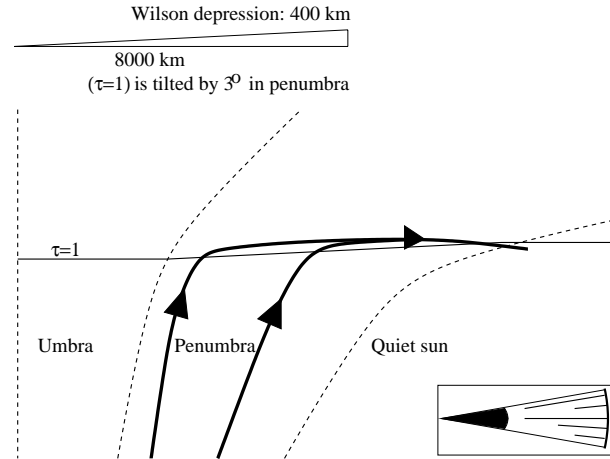


Fig. 11. Proposed flow geometry, sketched in a vertical cut through the spot. The surface of the penumbra is tilted by 3° , due to the Wilson depression. Sub-photospheric upflows in inner and mid penumbra bend almost horizontally in deep penumbral photosphere. At the outer penumbral edge, the flow channels slightly incline downwards. The lower right box sketches an azimuthal sector of the spot and illustrates the azimuthal and radial positions of flow channels.

resulting mean inclination is an average of a horizontal and a highly inclined flow component. At the outer penumbral boundary each flow channel bends slightly downwards and disappears. In Fig. 11 we have sketched two flow channels in a vertical cut through the spot. The box in the lower right corner of that figure depicts a circle sector of the spot as seen from above. The radial lines represent 5 flow channels with footpoints at different radial distances within the penumbra and illustrate the azimuthal spacing of the flow channels. Such a flow field is consistent with our observation. Moreover, it explains the observed increase of the line asymmetry with the formation height and the concomitant decrease of the line core shift (c.f., Stellmacher & Wiehr 1980). Furthermore, it explains, why the Evershed effect ceases abruptly at the outer penumbral edge.

5.3. Consistency with theoretical models

In our proposed flow geometry, plasma enters the photosphere at the footpoint of each channel. Since we observe a correlation between upflow and intensity, the upflows are hot and give rise to penumbral grains, just as in the moving tube model of Schlichenmaier et al. (1998b). The picture of hot upflow channels is further supported by Johannesson (1993) and Rimmele (1995) who report on blue-shifted line profiles that stem from penumbral grains, indicating an upflow velocity of 100–200 m s^{-1} . In the moving tube model the hot plasma cools radiatively as it flows radially outwards in very deep photospheric layers. The flow velocities that we infer from our observation are smaller than those predicted by the model ($v > 10 \text{ km s}^{-1}$). This is in accordance with our expectation, since (i) we only measure the azimuthal mean of the velocity and (ii) the contribution function is wider than the flow channel itself (cf., Sect. 1). Hence, as far as the inner and the mid penumbra is concerned,

the proposed flow geometry is consistent with the moving tube model.

At the outer penumbral boundary the plasma flow of the model continues along the magnetopause and slowly ascends up into the sunspot canopy. This is a clear discrepancy with our observations which show the presence of a downflow.

Downflows at the outer penumbral boundary are predicted by the siphon flow model (see e.g. Montesinos & Thomas 1997, for the most recent modeling), in which the flow channel consists of a magnetic arch that has an upstream footpoint within the penumbra and a downstream footpoint at the outer penumbral boundary. However, even though this model predicts downflows at the outer penumbral edge, it seems to be inconsistent with other observational aspects: 1) The observations of low lying flow channels are a strong argument against the siphon flow models, since in these models the flux tube arch reaches out to a height of several 100 km. 2) Moreover, that model is only capable to explain footpoint separations of not more than 1500 km. Instead, our observation indicates that the up- and downstream arches should be capable to span the whole penumbra, i.e. in our case up to 8000 km. 3) The siphon flow model also suffers from the fact that it only operates if the magnetic field strength at the inner footpoint is smaller than the magnetic field strength at the outer footpoint.

5.4. Vertical velocity beyond outer edge of penumbra

In our data the azimuthal mean value of the velocity in the vicinity of the sunspot is smaller than the convective blue-shift of the quiet sun granulation (cf., Fig. 7). In an annulus of a width up to 10 Mm, the azimuthal mean rises continuously until it reaches the more or less constant value of the convective blue-shift. This observation agrees with previous work (Nesis et al. 1989, 1996; Title et al. 1992) which found a significantly suppressed vertical velocity component in plages. We surmise that the suppressed convective blue-shift is the consequence of “abnormal” granulation. Possibly, the abnormal granulation is a consequence of magnetic flux that diffuses away from the spot to form the sunspot moat.

5.5. Final remarks

In this work, we made a compromise: in order to distinguish between horizontal and vertical velocity components, we needed to take the azimuthal average of the velocity field. Thereby we spatially averaged over the penumbral fine structure (that we actually resolved), and we studied the flow geometry of the mean flow field. Obviously, the aim must be to study the flow field of each individual physical entity, i.e. *filament*. Then of course one faces the problem of being unable to distinguish between the vertical and horizontal velocity component, since only the line-of-sight component can be measured.

Measuring the magnetic field may help to determine the flow direction if one assumes that the flow is locally parallel to the magnetic field lines (frozen field). However, since different magnetic components are present in the penumbral atmosphere

it would be an extremely difficult task to identify the polarized part that originates in a certain flow channel. The issue is further complicated by the fact that most visible spectral lines that are suitable for measurements of the magnetic field vector are formed in the mid photosphere and do not provide information about flow channels deep in the photosphere.

Many predictions from the moving tube model are confirmed by our observations, except for the flow inclination at the outer penumbral boundary. But the moving tube model provides additional predictions of observable quantities, e.g. the magnetic field strength should be reduced within the upflow channels, and be of the same strength as the surrounding plasma in the outer horizontal part of the tube. Recently, Rüedi et al. (1999) have reported on observations indicating that the cool part of the flow is associated with weak magnetic fields. In that respect further observational evidence as well as further theoretical modeling, i.e. investigation of the dynamical behavior of flux tubes that have a downstream arch at the outer edge of the penumbra, is needed to learn more about the nature of the penumbra.

Acknowledgements. Part of this work was supported by the *Deutsche Forschungsgemeinschaft, DFG*. We are indebted to Dr. U. Grossmann-Doerth who calculated synthetic line profiles and Dr. H. Schleicher who supplied atmospheric models. We thank Dr. T. Kentischer for his patient support during the TESOS observations, H. Schilling for technical assistance at the VTT, and Dr. A. Nesis for useful comments on the manuscript. This research has made use of NASA's Astrophysics Data System Abstract Service.

References

- Balthasar H., 1984, *Solar Phys.* 93, 219
- Balthasar H., Schleicher H., Bendlin C., Volkmer R., 1996, *A&A* 315, 603
- Balthasar H., Schmidt W., Wiehr E., 1997, *Solar Phys.* 171, 331
- Börner P., Kneer F., 1992, *A&A* 259, 307
- Bumba V., 1960, *Izv. Kryms. Astrofiz. Observ.* 23, 212
- Denker C., 1998, *Solar Phys.* 180, 81
- Ding M.D., Fang C., 1989, *A&A* 225, 204
- Evershed J., 1909, *MNRAS* 69, 454
- Grossmann-Doerth U., 1994, *A&A* 285, 1012
- Grossmann-Doerth U., Schmidt W., 1981, *A&A* 95, 366
- Holmes J., 1963, *MNRAS* 126, 155
- Holweger H., Müller E., 1974, *Solar Phys.* 39, 19
- Ichimoto K., 1987, *PASJ* 39, 329
- Ichimoto K., 1988, *PASJ* 40, 103
- Johannesson A., 1993, *A&A* 273, 633
- Kentischer T., Schmidt W., Sigwarth M., v. Uexküll M., 1998, *A&A* 340, 569
- Maltby P., 1964, *Astrophysica Norvegica* 8, 205
- Montesinos B., Thomas J.H., 1997, *Nat* 390, 485
- Nesis A., Fleig K.-H., Mattig W., 1989, In: Rutten R.J., Severino G. (eds.) *Solar and Stellar Surface Granulation*. NATO ASI Series. Serie C, Mathematical and physical sciences: Vol. 263, Kluwer, Dordrecht, p. 289
- Nesis A., Hammer R., Hanslmeier A., et al., 1996, *A&A* 310, 973
- Rimmele T., 1995, *A&A* 298, 260
- Rüedi I., Solanki S.K., Keller C.U., 1999, *A&A* 348, L37

- Schlichenmaier R., Schmidt W., 1999, A&A 349, L37 (paper I)
Schlichenmaier R., Jahn K., Schmidt H.U., 1998a, ApJ 493, L121
Schlichenmaier R., Jahn K., Schmidt H.U., 1998b, A&A 337, 897
Schmidt W., Kentischer T., 1995, A&AS 113, 363
Schröter E.H., 1965, Zeitschrift f. Astrophysik 62, 228
Schröter E.H., 1967, In: Xanthakis J.N. (ed.) Solar Physics. John Wiley & Sons, London, p. 325
Servajean R., 1961, Ann. Astrophys. 23, 1
Shine R.A., Title A.M., Tarbell T.D., et al., 1994, ApJ 430, 413
Solanki S.K., Montavon C.A.P., Livingston W., 1994, A&A 283, 221
Solanki S.K., Finsterle W., Rüedi I., Livingston W., 1999, A&A 347, L27
Stanchfield II D.C.H., Thomas J.H., Lites B.W., 1997, ApJ 447, 485
Stellmacher G., Wiehr E., 1980, A&A 82, 157
Sütterlin P., Wiehr E., 1998, A&A 336, 367
Title A.M., Topka K.P., Tarbell T.D., et al., 1992, ApJ 393, 782
Title A.M., Frank Z.A., Shine R.A., et al., 1993, ApJ 403, 780
Westendorp Plaza C., del Toro Iniesta J.C., Ruiz Cobo B., et al., 1997, Nat 389, 47
Wiehr E., 1994, A&A 298, L17
Wiehr E., 1996, A&A 309, L4
Wiehr E., Degenhardt D., 1994, A&A 287, 625